

Research Article

Numerical and Experimental Study on End Effect of Waste-Soil Samples under Uniaxial Compression

Yukai Wang ¹, Xiaoli Liu ¹, and Bo Pang ²

¹State Key Laboratory of Hydrosience and Engineering, Tsinghua University, Beijing 100084, China

²Information Institute, Ministry of Emergency Management of the People's Republic of China, Beijing 100029, China

Correspondence should be addressed to Yukai Wang; wangyukai@mail.tsinghua.edu.cn

Received 12 January 2022; Revised 16 February 2022; Accepted 28 February 2022; Published 17 March 2022

Academic Editor: Yang Yu

Copyright © 2022 Yukai Wang et al. This is an open access article distributed under the Creative Commons Attribution License, which permits unrestricted use, distribution, and reproduction in any medium, provided the original work is properly cited.

In order to investigate the influence of end effect on the waste-soil sample strength under uniaxial compression, the influence law of end effect on the uniaxial compression strength is numerically simulated by the FLAC^{3D} software, and the reliability of the numerical model is verified by comparing it with the test results. Based on the above model, the influence of end effect on the lateral displacement and stress state of waste-soil samples is simulated, and the formation mechanism of end effect under uniaxial compression is revealed. The results show that, when the friction coefficient increases from 0 to 0.4, the uniaxial compression strength and percentage of triaxial compression units first increase rapidly and then slowly and then finally remain invariant. With the increase of the friction coefficient, the lateral displacement of the sample is significantly reduced. On the end surface, the nearer to the edge one is, the greater the decrease is. The triaxial compression region on the axis section is triangular in distribution; with the increase of the friction coefficient, this region increases first rapidly and then slowly and then finally remains invariant. The end effect produces lateral compression stress by reducing the lateral displacement of the end surface of samples, and lateral compression stress causes the sample to enter the triaxial compression state. With the increase of the friction coefficient, the triaxial compression region increases gradually, and thus, the uniaxial compression strength of the entire sample increases.

1. Introduction

A waste dump is an important part of the open-pit mining, whose component materials are the topsoil and rock removed during open-pit mining, and it sometimes includes recoverable surface ores and lean ores [1, 2]. In recent years, disasters of different scales have occurred in many open-pit mine waste dumps, such as Dagushan iron ore [3], Basundhara coal mine [4], and “South Field” lignite mine [5], which has caused different economic losses and even casualties. The uniaxial compression strength of waste-soil is the most important factor in determining the dump stability, so an accurate measurement of uniaxial compressive strength of waste-soil sample is essential [6, 7]. However, because of the friction between the bearing plate and waste-soil sample in the uniaxial compression experiment, the uneven stress distribution, triaxial compression region, and tensile region will arise locally [8, 9]. The above phenomena will have a

bad effect on the accurate measurement of waste-soil sample parameters and the study of the failure mechanism [10]. Therefore, it is of great significance to study the end effect of waste-soil samples under uniaxial compression.

Many scholars have conducted theoretical and experimental studies on the process of the end effect under uniaxial compression. Liang et al. [11] studied the end effect and failure mode and found that K_p had similar effects as K_s while K_n had relatively less influence on the failure strength. Yu et al. [12] found that the effect of end friction on strength is weakened to a certain extent by reducing the friction coefficient between the indenter and the end face of the specimen. Xu et al. [13] studied the influence of the end effect on rock strength in true triaxial compression and conducted that any enhancement to the rock strength with the increase of σ_2 can be attributed to the end effect. Pan et al. [14] simulated the failure process under uniaxial compression with EPCA2D and found that the attempt to improve the

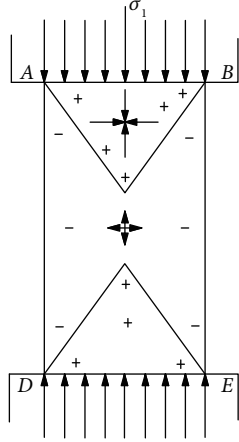


FIGURE 1: Stress distribution of waste-soil sample in uniaxial compression.

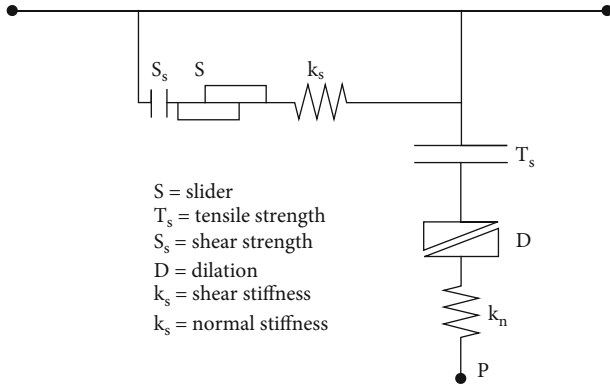


FIGURE 2: Components of the interface constitutive model. (Note: this figure is reproduced from Shuwei Sun et al. 2016.)

experimental quality by reducing the frictions was unreliable. Feng et al. [15] revealed the influence mechanism of end effect in a true triaxial compression test. Hou et al. [16] used FLAC^{3D} to simulate the failure process under uniaxial compression and found that the end effect made the axial stress at the end surface of the sample present a parabolic distribution. Jin et al. [17] simulated the dynamic compression behavior of the concrete under low strain rate conditions and found that the end effect changed the uniaxial stress state and damage distribution of the concrete, which improved the uniaxial compression strength obviously. Shi and Li [18] conducted true triaxial simulation experiments and came to the conclusion that the end effect could produce false intermediate principal stress to increase the maximum failure stress. Liu et al. [19] discussed the evolutionary rule of flaws in rock and its effect on the macromechanical uniaxial compression strength (UCS).

In general, the existence of the end effect in uniaxial compression experiments has been confirmed by many scholars and experts. However, research on the formation mechanism and influence process of the end effect is limited. To further study the formation mechanism of the end effect, a uniaxial compression model under different friction coeffi-

cients is established firstly. Then, through uniaxial compression experiments, the variation law of uniaxial compression strength with friction coefficient is obtained, and the reliability of the model is verified. On this basis, the present paper uses a numerical simulation method to study the stress-strain state of waste-soil samples, and the formation mechanism and influence process of the end effect are summarized. The objectives of this paper are the following: (1) to obtain the variation law of uniaxial compression strength with friction coefficient; (2) to discover the stress-strain state of waste-soil samples under different friction coefficients; and (3) to reveal the formation mechanism of the end effect in uniaxial compression. The main contribution of this study is revealing the formation mechanism, evolutionary process, critical friction coefficient, and failure pattern of the end effect under uniaxial compression, which provides a reference for reducing and eliminating the end effect.

2. Problem Description and Methodology

2.1. Problem Description. The problem description is given in Figure 1. During the uniaxial compression of the waste-soil sample, the uncoordinated deformation between the waste-soil sample and bearing plate is caused by the friction between them, which results in the formation of a stress hoop on the end surface and the rise of a “funnel-shaped” stress area (see Figure 1) [20]. Due to the horizontal constraint on the end surface of waste-soil samples, the compression stress (+) is formed in two triangular areas that contact the bearing plates AB and DE. Due to the decrease of the end constraint, the tensile stress (-) is formed in the middle part of the waste-soil sample [21]. The above uneven stress distribution will lead to the increase of the uniaxial compression strength of waste-soil samples, which will bring adverse effects on the accurate measurement of waste-soil sample parameters and the study of the rock failure mechanism.

2.2. Simulation of Sample-Plate Interface. Compared with other mechanical models, a linear Coulomb shear strength model can better simulate the transfer of stress and deformation between different material interfaces, so the interfaces between samples and plates are characterized by a linear Coulomb shear strength model in this study [22–24]. Interfaces have the properties of friction, cohesion, dilation, normal and shear stiffness, and tensile and shear bond strength. Figure 2 illustrates the components of the constitutive model acting at an interface node (P).

The normal and shear forces that describe the elastic interface response are determined by the following equations:

$$\begin{aligned} F_n^{(t+\Delta t)} &= k_n \mu_n A + \sigma_n A, \\ F_{si}^{(t+\Delta t)} &= F_{si}^{(t)} + k_n \Delta \mu_{si}^{(t+(1/2)\Delta t)} A + \sigma_{si} A, \end{aligned} \quad (1)$$

where $F_n^{(t+\Delta t)}$ and $F_{si}^{(t+\Delta t)}$ are the normal and shear force at time $(t + \Delta t)$, respectively, μ_n is the absolute normal penetration of the interface node into target face, $\Delta \mu_{si}$ is the

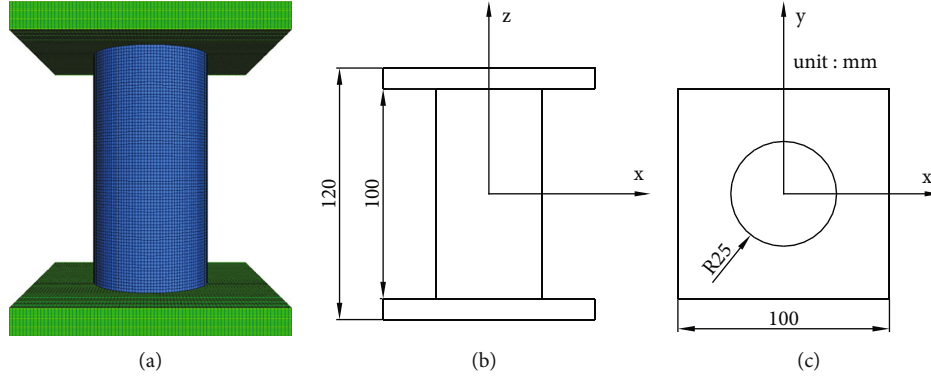


FIGURE 3: Numerical model. (a) Three-dimension view. (b) Elevation view. (c) Top view.

TABLE 1: Table of mechanical parameters of the model.

Material	Bulk modulus (Pa)	Shear modulus (Pa)	Cohesion (MPa)	Friction angle (°)	Dilation angle (°)
Waste-soil sample	2×10^2	1×10^2	2.558	36	10
Bearing plate	2×10^5	1×10^5			

TABLE 2: Table of mechanical parameters of the contact surface.

Material	Cohesion (MPa)	Friction angle (°)	Normal stiffness (GPa m^{-1})	Tangential stiffness (GPa m^{-1})
Contact surface	0	0-27	0.2	0.2

incremental relative shear displacement vector, k_n and k_s are the normal and shear stiffness, respectively, σ_n is the additional normal stress added due to interface stress initialization, σ_{si} is the additional shear stress vector due to interface stress initialization, and A is the representative area associated with an interface node.

In this study, the use of an interface element covers the sample-plate separation, and nonlinear analysis is carried out; the value for the interface stiffness should be high enough to minimize the contribution of those elements to the accumulated displacements. A good rule-of-thumb is that k_n and k_s should be set to at least ten times the equivalent stiffness of the stiffest neighboring zone [25]. To satisfy this requirement, k_n and k_s for the interface elements are both set equal to 0.2 GPa m^{-1} in the current analyses. These values were also adopted by Comodromos and Papadopoulos [26] in their benchmark test on interface elements.

2.3. Modeling of Uniaxial Compression. The numerical model uses cylindrical waste-soil samples with dimensions of $50 \text{ mm} \times 100 \text{ mm}$; the bearing plate's size is $100 \text{ mm} \times 100 \text{ mm} \times 10 \text{ mm}$ [27]. As shown in Figure 3, the blue part represents the waste-soil sample, whereas the green part indicates the bearing plate; the coordinate origin is located at the geometric center of the specimen. These two media, with 483003 grid-points and 460800 zones, compose the calculation model [28, 29]. The interface between the bearing plate and the waste-soil sample is used to simulate the

roughness between the bearing plate and the waste-soil sample [30]. The tangent of the internal friction angle of contact surfaces changes within 0~0.5, and the variation gradient is 0.1. In the numerical simulations, the sample loading mode is uniform distribution displacement loading on the bottom surface with a loading speed of $1.2 \times 10^{-6} \text{ m/step}$. The Mohr-Coulomb failure criterion is adopted as the calculation principle. Tables 1 and 2 list the model calculation parameters [31, 32]. The cohesive forces of the waste-soil sample and contact surface are expressed by C_s and C_c , respectively, and the internal friction angle of the waste-soil sample and contact surface are expressed by φ_s and φ_c , respectively.

In numerical calculations, the axial force is determined using the integral approach at the location with the same z -coordinate. The axial force is divided by the cross-sectional area to determine the axial stress [33–35]. Peak points of stress-strain curves are selected as failure points to study the relationship between the end effect and the uniaxial compression strength.

3. Validation of the Calculation Model

First, uniaxial compression strengths of waste-soil samples under the different friction coefficients are measured by uniaxial compression tests in this paper. Then, the reliability of the numerical analysis model and analysis method is verified by comparing the consistency between the test results and the simulation results [36, 37]. On this basis, the formation mechanism of the end effect is studied by numerical simulation.

3.1. Materials. The chemical composition of test soil samples has a great influence on the friction coefficient between the end surface and the waste-soil sample. The friction coefficient needs to be measured accurately to verify the reliability of the numerical model; it is necessary to give the chemical composition in detail. Three kinds of materials including



FIGURE 4: The (a) waste-soil and (b) binder used in this test.

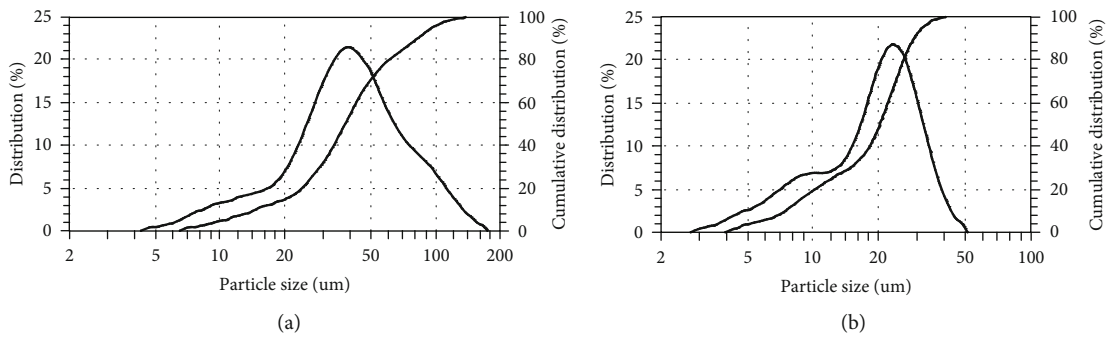


FIGURE 5: Particle size distribution of (a) waste-soil and (b) binder.



FIGURE 6: Samples.

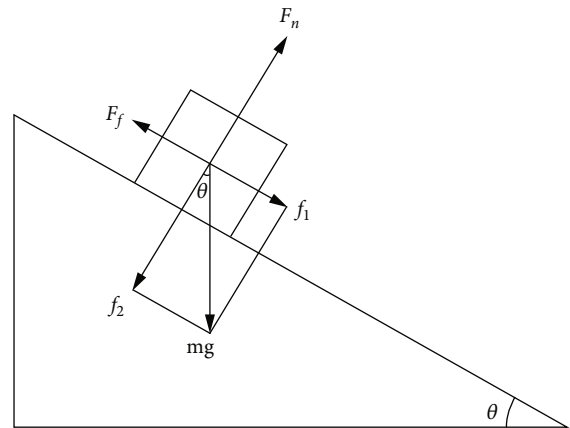


FIGURE 7: Sketch map of slope balance method.

the waste-soil, binder, and water were used in this research. The waste-soil utilized in this study is from a gold ore process plant of Guizhou Jinfeng Mining Limited (see Figure 4(a)), its absolute density is 2.59 t/m^3 , its packing density is 1.6 t/m^3 , its stopping angle is 35° , and its water content is less than 0.25% , so it can be identified as dry sand. The mineral composition of the waste-soil mainly includes quartz, chlorite, calcite, diopside, and a small amount of gypsum, pyrite, and sericite. The chemical composition of the waste-soil mainly includes SiO_2 , Al_2O_3 , CaO , FeO , and MgO . The particle size distribution of the waste-soil measured by the LS-C(IIA)-type laser particle sizer at China

University of Mining and Technology (Beijing) is shown in Figure 5(a). The effective particle sizes of the waste-soil are $D_{10} = 14.55 \mu\text{m}$, $D_{30} = 26.6 \mu\text{m}$, $D_{90} = 82.3 \mu\text{m}$, and $D_{97} = 106.71 \mu\text{m}$; the constrained particle size is $D_{60} = 54.27 \mu\text{m}$; the medium size $D_{50} = 38.30 \mu\text{m}$; the nonuniformity factor is $\varphi = 3.73$; and the curvature coefficient is $C_u = 0.896$, so the waste-soil belongs to the fine-grained soil.

The binder used in this study is the Portland cement of 32.5 MPa (P.O. 32.5, see Figure 4(b)). The chemical composition of the binder mainly includes CaO , SiO_2 , Al_2O_3 , Fe_2O_3 , and MgO . The particle size distribution of the binder



FIGURE 8: TYE-300D type test machine.

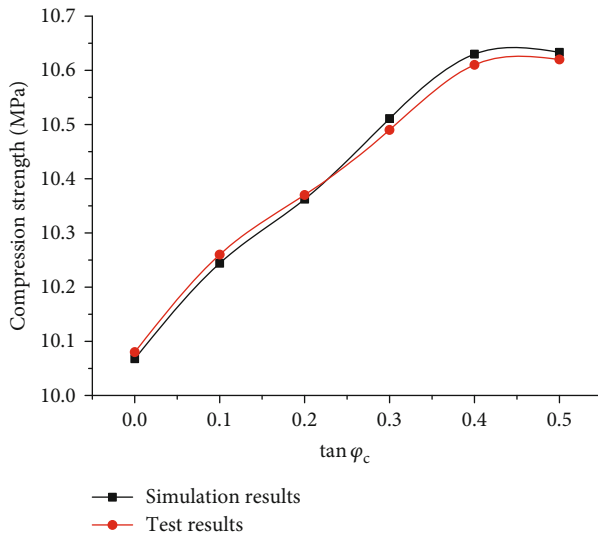


FIGURE 9: Uniaxial compression strength curve.

is shown in Figure 5(b). The effective particle sizes of the binder are $D_{10} = 7.48 \mu\text{m}$, $D_{30} = 12.26 \mu\text{m}$, $D_{90} = 29.60 \mu\text{m}$, and $D_{97} = 34.54 \mu\text{m}$; the constrained particle size is $D_{60} = 25.30 \mu\text{m}$; the medium size is $D_{50} = 20.39 \mu\text{m}$; the non-uniformity factor is $\varphi = 3.38$, and the curvature coefficient is $C_u = 0.794$. The water used in this study is common tap water.

3.2. Sample Preparation. The process of waste-soil sample preparation can be divided into three main parts: mortar mixing, molding, and sample maintenance [38–42]. (1) Pour the waste-soil and cementing agent into the mixing pot and stir evenly, and then add tap water into the mixing pot and stir evenly again. The mass ratio of water, cementing agent, and waste-soil is 7.6:1:10. Stir the slurry with a 5K5SS-type lifting multifunction mixer at low speed for 2 minutes, and then pause for 1 minute. Scrape the slurry on the mixing blades and on the wall of the mixing pot into the mixing pot, and then upturn the bottom slurry. Stir the slurry at high speed for 4 minutes. Complete the mixing and close the machine. (2) Pour the uniform-mixed slurry into the cylindrical test mold. The diameter of the cylindrical test mold is 5 cm, and the height is 10 cm. Then, tamp the slurry with

a tamping bar along the periphery of the test mold. Each waste-soil sample is tamped 30 times, and 20 instances of manual vibration are needed to drive out the bubbles in the slurry. Then, take a small amount of slurry to fill up the test mold, use a small scraper to smooth the surface, seal the test mold with a plastic cover, and seal the plastic cover with waterproof tape to prevent evaporation of the water in the mold. The test mold is finished and placed in a horizontal position. (3) Place the test mold in the thermostat box with a temperature of $20 \pm 1^\circ\text{C}$ and a relative humidity $\geq 90\%$. One day later, disassemble the test mold and remove the waste-soil sample, and then leave the waste-soil sample in the thermostat box for 28 days.

The waste-soil sample taken from the thermostat box may have an irregular shape because of the settlement phenomenon and small breakage during the process of taking out the block. Therefore, certain processing is needed, especially the upper section of the waste-soil sample, which needs to be smoothed with the metal scraper, to ensure that the load applied to the waste-soil sample is uniform when the mechanical properties are tested. Put the rapidly processed waste-soil sample into a sealed bag to limit the humidity change. Test waste-soil samples are shown in Figure 6.

3.3. Experiment Scheme. In the uniaxial compression test, the friction coefficient between the end surface and the waste-soil sample is adjusted by changing the surface roughness of the bearing plate and applying different types of lubricating oil; the friction coefficient is measured by the slope balance method (see Figure 7) [43, 44]. The gravity, slope support force, and friction force of the waste-soil sample are expressed by mg , F_n , and F_f , respectively; f_1 and f_2 are the components of the gravity along and perpendicular to the slope, respectively. For testing convenience, a cube waste-soil sample with a size of 4 cm is adopted to measure the friction coefficient. Adjust the slope (bearing plate) angle (θ) to ensure that the waste-soil sample is in the critical sliding state, at which point there are

$$\begin{aligned} F_f &= f_1 = mg \sin \theta, \\ F_n &= f_2 = mg \cos \theta, \\ F_f &= \mu F_n, \end{aligned} \quad (2)$$

So the conclusion of $\mu = \tan \theta$ is drawn. Due to the limitations of the experimental conditions, the case of $\mu = \tan \theta = 0.02$ is considered a complete smooth contact.

The uniaxial compression experiment was carried out using a TYE-300D-type cement mortar compression bending test machine (see Figure 8) at China University of Mining and Technology (Beijing), and the loading rate is 0.1 kN/s. In the process of testing, the test machine can record the load applied to the waste-soil sample at any time. When the waste-soil sample suddenly breaks down, the maximum load of the waste-soil sample is recorded, the test machine shuts down automatically, and the corresponding strength is the uniaxial compression strength of the waste-soil sample [45].

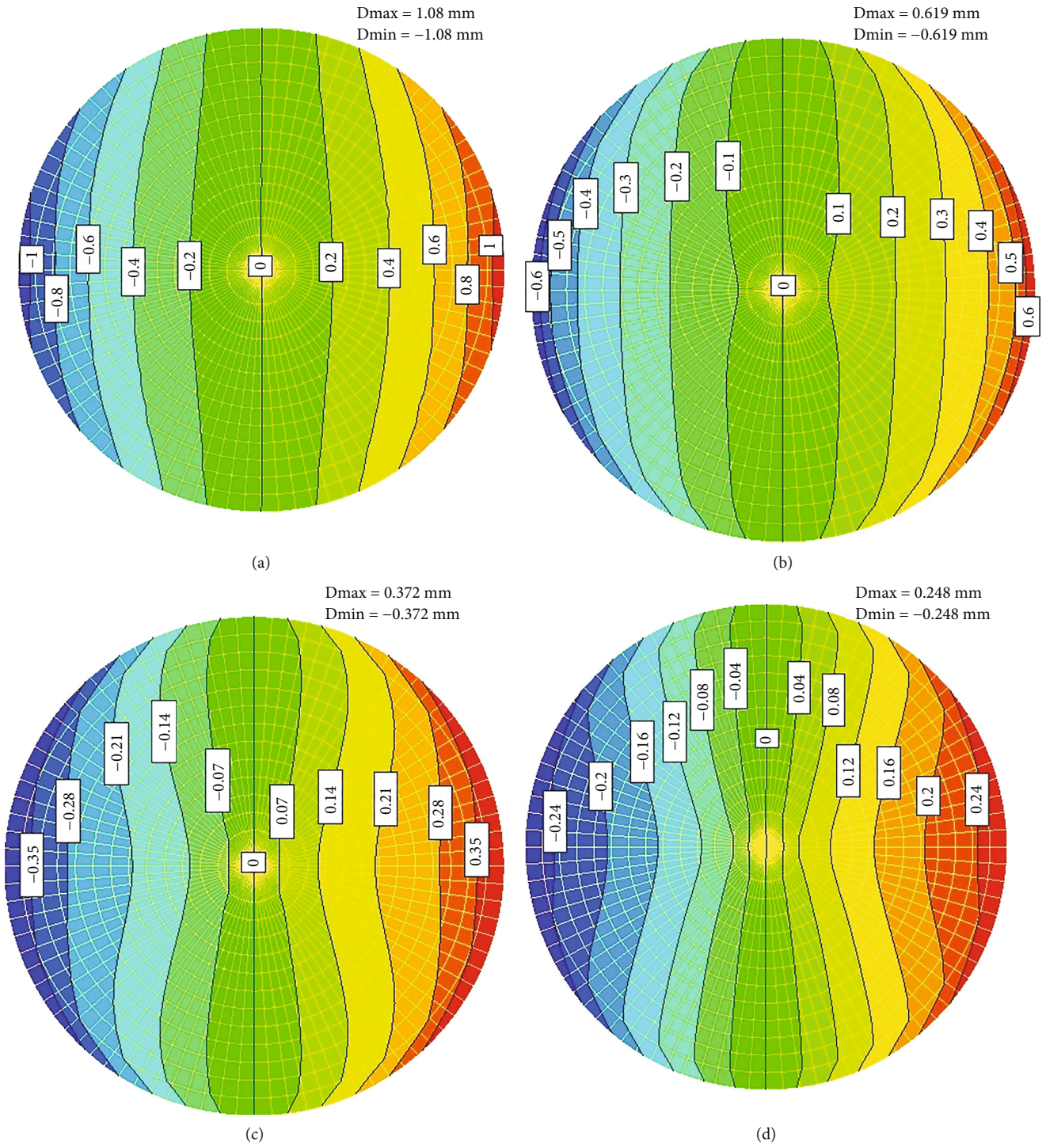


FIGURE 10: Continued.

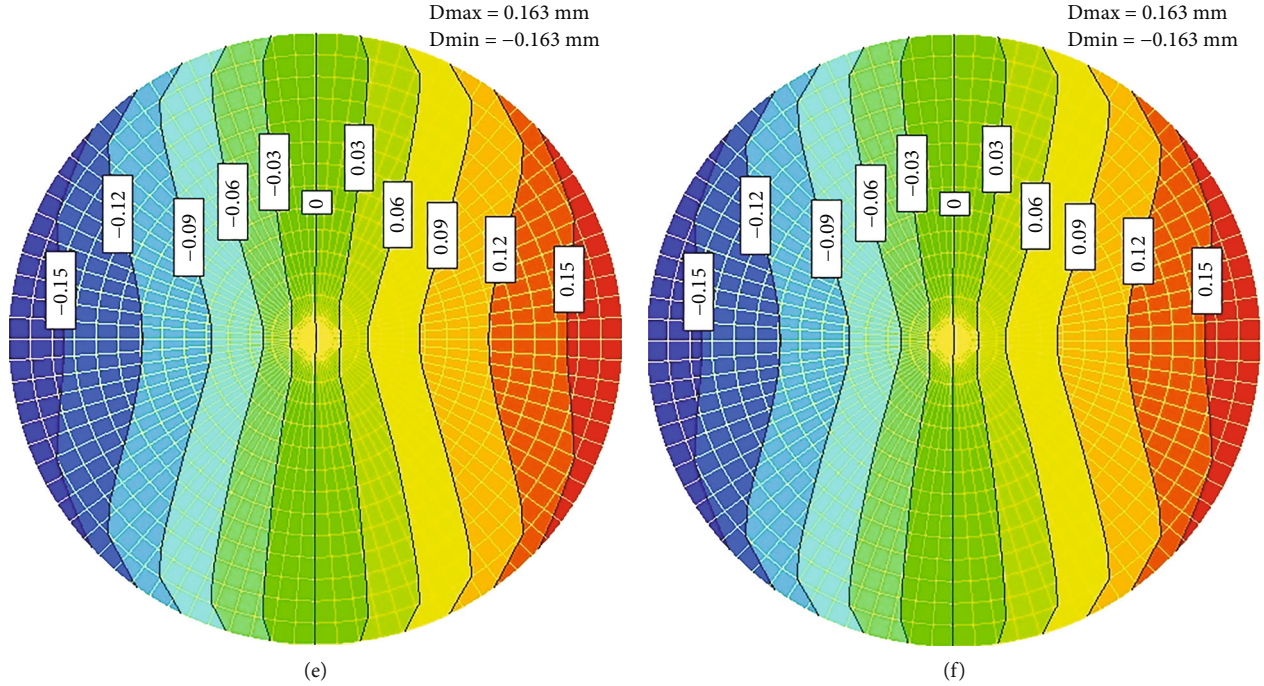


FIGURE 10: Isoline of lateral displacement. (a) $\tan \varphi_c = 0$. (b) $\tan \varphi_c = 0.1$. (c) $\tan \varphi_c = 0.2$. (d) $\tan \varphi_c = 0.3$. (e) $\tan \varphi_c = 0.4$. (f) $\tan \varphi_c = 0.5$.

3.4. *Test Results.* Figure 9 shows the uniaxial compression strength of waste-soil samples with the friction coefficient varying from 0 to 0.5. When the end surface of the waste-soil sample is smooth ($\tan \varphi_c = 0$), the uniaxial compression strength is 10.06 MPa. When the friction coefficient is within the range 0-0.4, the uniaxial compression strength sharply increases from 10.06 MPa to 10.6 MPa with the increase of the friction coefficient. After the friction coefficient reaches 0.4, the uniaxial compression strength remains 10.6 MPa invariantly, and the end friction has no further influence on the uniaxial compression strength. The curve slope initially remains invariant and then gradually decreases to 0. The maximum slope of the curve is 1.39 MPa, which indicates that, when the friction coefficient increases by 1%, the compression strength increases by 13.9 kPa. The result of the uniaxial compression test is almost the same as that of the numerical analysis, which verifies the reliability of the numerical analysis model and analysis method. The uniaxial compression strength curve also indicates that the end effect enhances the axial load capacity of the waste-soil samples significantly.

4. Calculation Results

4.1. *Influence of End Effect on Lateral Displacement.* The end effect directly affects the lateral displacement at the end of the waste-soil sample. Figure 10 shows the lateral displacement of the waste-soil sample with the coordinate of $z = -50$ mm. When the end surface is smooth ($\tan \varphi_c = 0$), the lateral displacement of each node on the end surface is outward along the radius; the displacement isoline is a set of vertical parallel lines with uniform distribution. The closer to the center of the end surface one is, the smaller the lateral dis-

placement is; the lateral displacement increases with the increase of distance from the center point, with the maximum displacement of 1.08×10^{-3} m. With the increase of the friction coefficient, isolines near the center first concave inward, forming a W shape; then, marginal isolines concave inward, forming a set of contour lines with a W shape. As the friction coefficient increases from 0 to 0.4, the displacement of each node of the end surface decreases; the maximum lateral displacement decreases from 1.08×10^{-3} m to 1.63×10^{-4} m. After the friction coefficient reaches 0.4, the end friction has no further influence on the lateral displacement. This phenomenon indicates that the end friction significantly prevents lateral deformation of the waste-soil sample; the closer to the edge one is, the greater the influence of the end friction is.

4.2. *Influence of End Effect on Principal Stress State.* In this paper, the region where the maximum principal stress, the minimum principal stress, and the intermediate principal stress are compression stress is defined as the triaxial compression zone. The distribution of triaxial compression zones along the axis section is shown in Figure 11, and the green part represents the triaxial compression zone. When the end surface is smooth, all of the regions are almost tensile stress zones, and this is the reason why the failure mode of the waste-soil sample is columnar cleavage. When the friction coefficient varies from 0 to 0.4, the triaxial compression regions on the axial section are approximately two isosceles triangles whose apex angle is approximately 74° . Triaxial compression regions in a three-dimensional space are two cones whose bottoms are end surfaces of the waste-soil sample. With the increase of the friction coefficient, the base and height of the isosceles triangle increase,

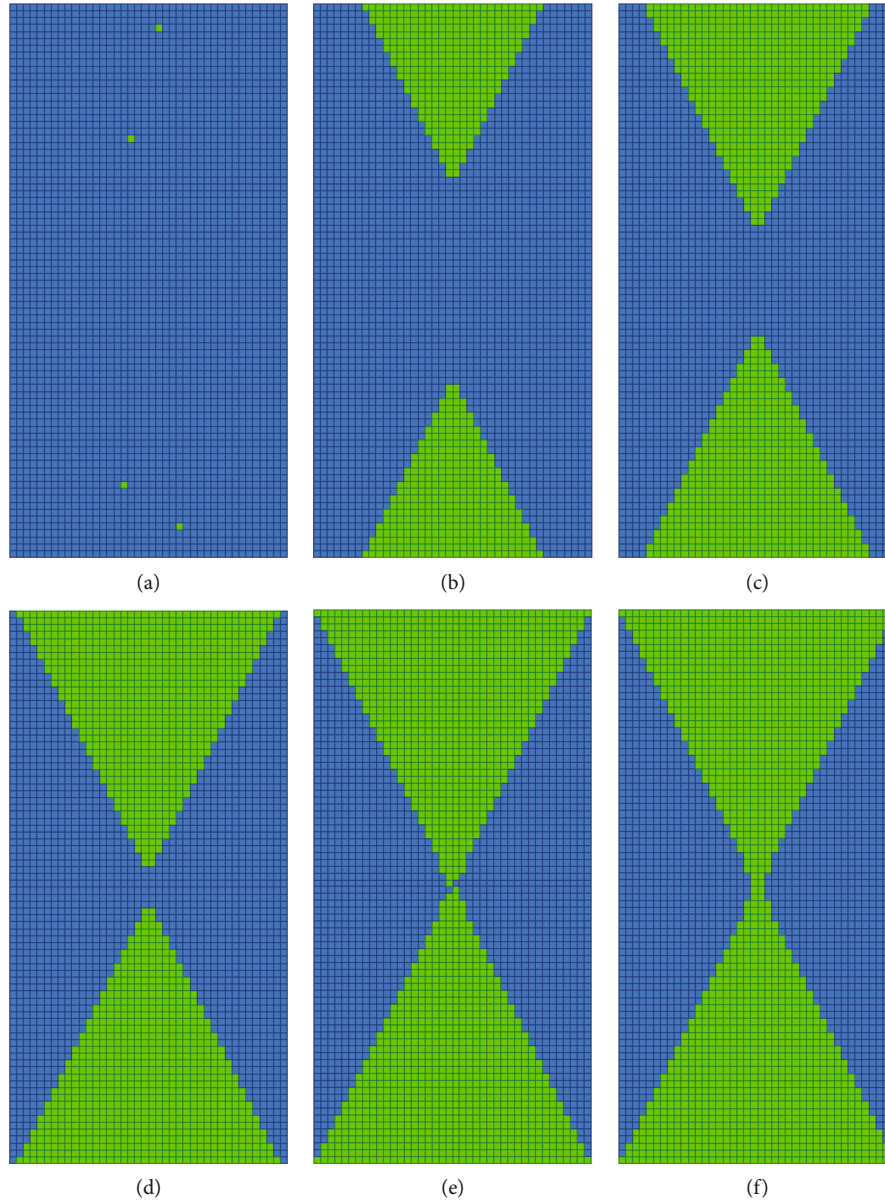


FIGURE 11: Distribution of triaxial compression area. (a) $\tan \varphi_c = 0$. (b) $\tan \varphi_c = 0.1$. (c) $\tan \varphi_c = 0.2$. (d) $\tan \varphi_c = 0.3$. (e) $\tan \varphi_c = 0.4$. (f) $\tan \varphi_c = 0.5$.

while the ratio of the height to the base remains constant. The increase rate of the height and base of the isosceles triangle gradually decreases to 0. When the friction coefficient reaches 0.4, the top and bottom triangles are joined together, and the triaxial compression zone remains unchanged. This is the reason why the failure mode of the waste-soil sample is transformed from columnar cleavage to conical shear fracture with the contact surface varying from smooth to rough.

In addition, the change of triaxial compression regions directly affects the number of triaxial compression units. In this paper, the change of triaxial compression units is described by the percentage of triaxial compression units to total units, and the number of triaxial compression units is counted by the homemade FISH function. The percentage of triaxial compression units is presented in Figure 12. When the end surface is smooth, there are almost no triaxial com-

pression units, and the percentage of triaxial compression units is essentially equal to 0. When the friction coefficient increases from 0 to 0.3, the percentage of triaxial compression units increases linearly, and the percentage value increases from 0 to 28.42%. When the friction coefficient increases from 0.3 to 0.4, the percentage of triaxial compression units shows an upward trend from 28.42% to 32.91%, but the increase rate gradually decreases to 0. After the friction coefficient reaches the threshold of 0.4, the percentage of triaxial compression units does not increase with the increase of the friction coefficient.

5. Analysis and Discussion

From the calculation results shown in Figures 9 and 12, uniaxial compression strength has a similar change tendency

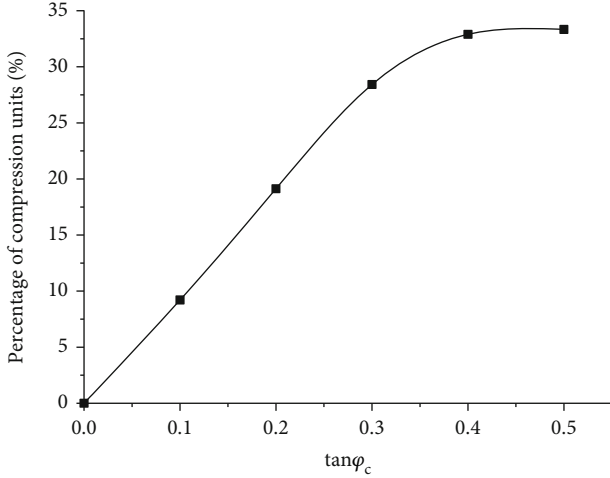


FIGURE 12: Percentage of triaxial compression units.

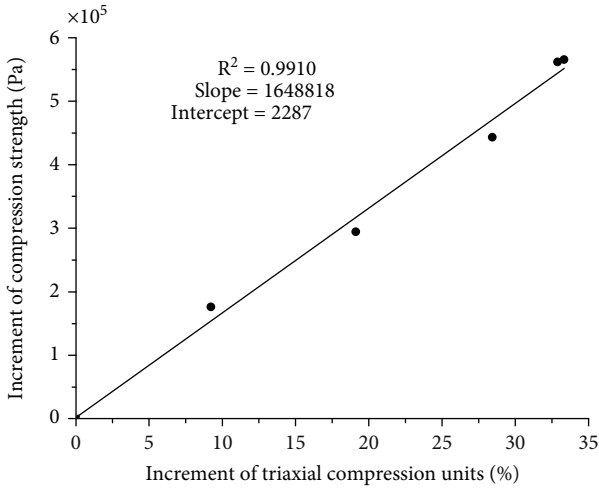


FIGURE 13: Increment between triaxial compression unit and compression strength.

with the percentage of triaxial compression units. The percentage increment of triaxial compression units and the uniaxial compression strength increment show an obvious linear relationship (see Figure 13). As shown in Figure 13, the vertical axis represents the increment of uniaxial compression strength between the rough and smooth end surface; the horizontal axis represents the increment of triaxial compression units between the rough and smooth end surface. Via linear fitting, the correlation coefficients of the simple fitting are determined to be equal to 0.991, which proves the reliability of the fitting. Figure 13 also shows that the corresponding slope is 1.6488 MPa, which indicates that, when the triaxial compression units increase by 1%, the uniaxial compression strength increases by 16.4882 kPa. This finding indicates that the end effect enhances the axial load capacity of the waste-soil samples by increasing the triaxial compression units.

The end effect directly reduces the lateral displacement near the end surface. The lateral compression stress (σ_3) is caused by restricting the lateral expansion of waste-soil samples, so the smaller the lateral displacement is, the greater the

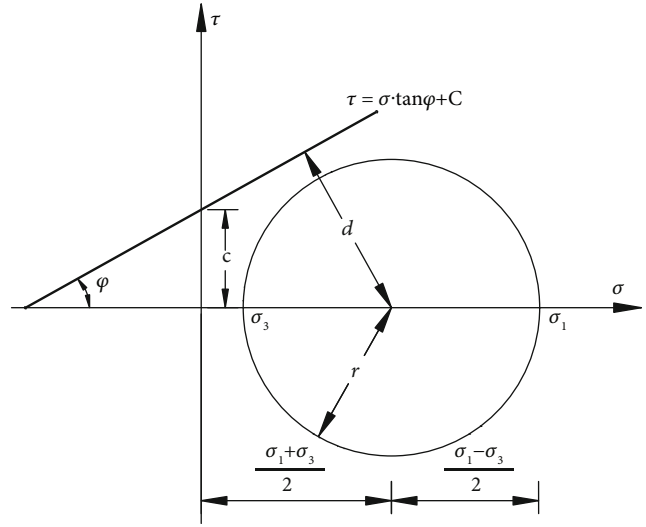


FIGURE 14: The Mohr strength curve and the Mohr circle.

lateral compression stress is. It is known from the lateral displacement distribution of waste-soil samples (see Figure 10) that, the closer to the end surface one is, the greater the lateral compression stress is; the greater the roughness of the contact surface is, the greater the lateral compression stress is. Accordingly, the principal stress state of samples under different contact surface parameters is shown in Figure 11. Compression stress is positive while tensile stress is negative in geotechnical mechanics, so the Mohr strength curve and Mohr circle can be described in Figure 14. The formulas for the Mohr circle and Mohr strength curve are $(\sigma - ((\sigma_1 + \sigma_3)/2))^2 + \tau^2 = (\sigma_1 - \sigma_3)^2/4$ and $\tau = \sigma \tan \phi + C$, respectively. When the distance from the Mohr circle's center to the strength curve is greater than the Mohr circle's radius, that is, $\Delta = d - r$, the waste-soil sample is in the elastic stage; otherwise, shear failure occurs in the waste-soil sample. By substituting rock mechanics parameters ($\phi_s = 36^\circ$ and $C_s = 2.558$ MPa) into the above equations, we can get $\Delta = 0.7939\sigma_3 - 0.2601\sigma_1 + 2.0694$. When the lateral stress (σ_3) is greater than 0, greater axial stress (σ_1) is required to make the Δ less than 0, so the lateral compression stress can improve the axial compression strength of the waste-soil sample. This is why the uniaxial compression strength and triaxial compression units have the same variation tendency and linear increments.

Through the above analysis, the formation mechanism of the end effect is described as follows. The end effect produces lateral compression stress by reducing the lateral displacement of the end surface of waste-soil samples, and the lateral compression stress makes the waste-soil sample locally enter the triaxial compression state. With the increase of the friction coefficient of the end surface, the triaxial compression region increases gradually, and thus, the uniaxial compression strength of the entire waste-soil sample is increased.

6. Conclusions

In this paper, the formation mechanism of the end effect in uniaxial compression was revealed through uniaxial

compression tests and by simulating the uniaxial compression process of cylindrical waste-soil samples under different contact surface parameters using a finite difference technique (FLAC^{3D}). The following findings are obtained:

- (1) When the friction coefficient increases from 0 to 0.3, the uniaxial compression strength linearly increases from 10.06 MPa to 10.52 MPa. When the friction coefficient increases from 0.3 to 0.4, the uniaxial compression strength gradually increases from 10.52 MPa to 10.6 MPa. After the friction coefficient reaches 0.4, the uniaxial compression strength remains invariant at 10.6 MPa
- (2) With the increase of the friction coefficient, the lateral displacement of the waste-soil sample decreases significantly. On the end surface of the waste-soil sample, the nearer to the edge one is, the greater the decrease is, and the isoline of the lateral displacement is transformed from a parallel line to a W-shaped curve
- (3) The triaxial compression region on the axis section is a triangle whose base is the end surface of the waste-soil sample. When the friction coefficient increases from 0 to 0.4, the triangle area increases first rapidly and then slowly. After the friction coefficient reaches the threshold of 0.4, the triaxial compression region remains constant. With the increase of the friction coefficient, the uniaxial compression strength and triaxial compression units have the same variation tendency and linear increments
- (4) The end effect produces the lateral compression stress by reducing the lateral displacement of the end surface of the waste-soil samples, and the lateral compression stress makes the waste-soil sample locally enter the triaxial compression state. With the increase of the friction coefficient of the end surface, the triaxial compression region increases gradually, and thus, the uniaxial compression strength of the entire waste-soil sample increases

Data Availability

All data used to support the findings of this study are included within the article.

Conflicts of Interest

The authors declare that they have no conflicts of interest.

Acknowledgments

This work was supported by the National Key Research and Development Plan (No. 2018YFC1504902), the National Natural Science Foundation of China (No. 52079068), and the State Key Laboratory of Hydrosience and Hydraulic Engineering (No. 2021-KY-04).

References

- [1] Y. Wang, S. Sun, B. Pang, and L. Liu, "Base friction test on unloading deformation mechanism of soft foundation waste dump under gravity," *Measurement*, vol. 163, no. 8, article 108054, 2020.
- [2] J. Wang and C. Chen, "Stability analysis of slope at a disused waste dump by two-wedge model," *International Journal of Mining, Reclamation and Environment*, vol. 31, no. 8, pp. 575–588, 2017.
- [3] Y. Wang, S. Sun, and L. Liu, "Mechanism, stability and remediation of a large scale external waste dump in China," *Geotechnical and Geological Engineering*, vol. 37, no. 6, pp. 5147–5166, 2019.
- [4] B. Poulsen, M. Khanal, A. Rao, D. Adhikary, and R. Balusu, "Mine overburden dump failure: a case study," *Geotechnical & Geological Engineering*, vol. 32, no. 2, pp. 297–309, 2014.
- [5] E. Steiakakis, K. Kavouridis, and D. Monopolis, "Large scale failure of the external waste dump at the "south field" lignite mine, northern Greece," *Engineering Geology*, vol. 104, no. 3–4, pp. 269–279, 2009.
- [6] Y. Bao, X. Han, J. Chen et al., "Numerical assessment of failure potential of a large mine waste dump in Panzhihua City, China," *Engineering Geology*, vol. 253, no. 4, pp. 171–183, 2019.
- [7] Y. Wang, S. Sun, B. Pang, and L. Liu, "Experimental study on unloading deformation mechanisms of soft base dumps of open-pit mines," *Chinese Journal of Rock Mechanics and Engineering*, vol. 39, no. 2, pp. 359–373, 2020.
- [8] Z. Li, J. Song, X. Du, and X. Yang, "Size effect of confined concrete subjected to axial compression," *Journal of Central South University*, vol. 21, no. 3, pp. 1217–1226, 2014.
- [9] J. Rimen and D. Arghya, "Size effect in FRP-confined concrete under axial compression," *Journal of Composites for Construction*, vol. 21, no. 6, 2017.
- [10] J. Dong and L. Shao, "Study of unsaturated compacted soil considering influence of end effect by triaxial test," *Chinese Journal of Rock Mechanics and Engineering*, vol. 29, no. 9, pp. 1937–1944, 2010.
- [11] Z. Liang, X. Wu, S. Tang, and W. Wang, "Numerical simulation on end effect of rock specimens based on the anisotropic interface element model," *Journal of Basic Science and Engineering*, vol. 26, no. 3, pp. 526–537, 2018.
- [12] J. Yu, Y. Wang, Q. Wang, Q. Zhu, and S. Fu, "Study of triaxial mechanical test based on MSV method for reducing end friction effect," *Journal of China Three Gorges University*, vol. 41, no. 5, pp. 59–64, 2019.
- [13] Y. Xu, M. Cai, X. Zhang, and X. Feng, "Influence of end effect on rock strength in true triaxial compression test," *Canadian Geotechnical Journal*, vol. 54, no. 6, pp. 862–880, 2017.
- [14] P. Pan, H. Zhou, and X. Feng, "Research on effect of loading conditions on failure processes of rocks with different sizes under uniaxial compression," *Chinese Journal of Rock Mechanics & Engineering*, vol. 27, no. 2, pp. 3636–3642, 2008.
- [15] X. Feng, X. Zhang, C. Yang, R. Kong, X. Liu, and S. Peng, "Evaluation and reduction of the end friction effect in true triaxial tests on hard rocks," *International Journal of Rock Mechanics & Mining Sciences*, vol. 4, no. 2, pp. 699–704, 2017.
- [16] H. Hou, S. Zhang, and G. Wu, "Influence of stress distribution regulation of sample ends on uniaxial compression with pad,"

- Journal of Anhui University of Science and Technology(Natural Science)*, vol. 35, no. 3, pp. 59–62, 2015.
- [17] L. Jin, Y. Han, Z. Ding, and X. Du, “Effect of end friction on the dynamic compressive mechanical behavior of concrete under medium and low strain rates,” *Journal of Vibration and Shock*, vol. 2016, no. 11, pp. 1–20, 2016.
- [18] L. Shi and X. Li, “Analysis of end friction effect in true triaxial test,” *Rock and Soil Mechanics*, vol. 30, no. 4, pp. 1159–1164, 2009.
- [19] X. Liu, S. Wang, E. Wang, J. Wang, and B. Hu, “Evolutionary rules of flaws in rock subjected to uniaxial compression and rock strength,” *Chinese Journal of Rock Mechanics and Engineering*, vol. 27, no. 6, pp. 1195–1201, 2008.
- [20] M. Shen and J. Chen, *Rock Mass Mechanics*, Tongji University Press, Shanghai, China, 2006.
- [21] J. Wang and S. Sun, *Open-pit mine slope engineering*, Science Press, Beijing, China, 2016.
- [22] S. Sun, W. Wang, and F. Zhao, “Three-dimensional stability analysis of a homogeneous slope reinforced with micropiles,” *Mathematical Problems in Engineering*, vol. 2014, Article ID 864017, 11 pages, 2014.
- [23] Q. Du, X. Liu, and E. Wang, “Strength reduction of coal pillar after CO₂ sequestration in abandoned coal mines,” *Minerals*, vol. 7, no. 2, p. 26, 2017.
- [24] S. Dai, X. Liu, and K. Nawnit, “Experimental study on the fracture process zone characteristics in concrete utilizing DIC and AE methods,” *Applied Sciences*, vol. 9, no. 7, p. 1346, 2019.
- [25] E. M. Comodromos and K. D. Pitilakis, “Response evaluation for horizontally loaded fixed-head pile groups using 3-D non-linear analysis,” *International Journal for Numerical and Analytical Methods in Geomechanics*, vol. 29, no. 6, pp. 597–625, 2005.
- [26] E. M. Comodromos and M. C. Papadopoulou, “Response evaluation of horizontally loaded pile groups in clayey soils,” *Geotechnique*, vol. 62, no. 4, pp. 329–339, 2012.
- [27] S. Sun, H. Lin, and L. Ren, *Application of FLAC3D in Geotechnical Engineering*, China Water and Power Press, Beijing, China, 2011.
- [28] H. Lin, P. Cao, and Y. Wang, “Numerical simulation of a layered rock under triaxial compression,” *International Journal of Rock Mechanics and Mining Sciences*, vol. 60, no. 6, pp. 12–18, 2013.
- [29] X. Fan, R. Chen, H. Lin, H. Lai, C. Zhang, and Q. Zhao, “Cracking and failure in rock specimen containing combined flaw and hole under uniaxial compression,” *Advances in Civil Engineering*, vol. 2018, Article ID 9818250, 15 pages, 2018.
- [30] S. Sun, F. Zhao, and K. Zhang, “Stability of slopes reinforced with truncated piles,” *Advances in Materials Science and Engineering*, vol. 2016, Article ID 1570983, 16 pages, 2016.
- [31] X. Sun, X. Fang, and L. Guan, *Mechanics of Materials*, High Education Press, Beijing, China, 2009.
- [32] J. Liu, “Simulation to the effects on strain localization due to end friction,” *Soil Engineering and Foundation*, vol. 20, no. 5, pp. 47–50, 2006.
- [33] H. Lin, Z. Xiong, T. Liu, R. Cao, and P. Cao, “Numerical simulations of the effect of bolt inclination on the shear strength of rock joints,” *International Journal of Rock Mechanics & Mining Sciences*, vol. 66, no. 1, pp. 49–56, 2014.
- [34] H. Sun, X. Liu, and J. Zhu, “Correlational fractal characterisation of stress and acoustic emission during coal and rock failure under multilevel dynamic loading,” *International Journal of Rock Mechanics and Mining Sciences*, vol. 117, no. 2, pp. 1–10, 2019.
- [35] X. Liu, G. Han, E. Wang, S. Wang, and K. Nawnit, “Multiscale hierarchical analysis of rock mass and prediction of its mechanical and hydraulic properties,” *Journal of Rock Mechanics and Geotechnical Engineering*, vol. 10, no. 4, pp. 694–702, 2018.
- [36] D. Yin, S. Chen, X. Liu, and H. Ma, “Simulation study on strength and failure characteristics for granite with a set of cross-joints of different lengths,” *Advances in Civil Engineering*, vol. 2018, Article ID 2384579, 10 pages, 2018.
- [37] C. Wang, Y. Zhao, Y. Zhao, and W. Wan, “Study on the interaction of collinear cracks and wing cracks and cracking behavior of rock under uniaxial compression,” *Advances in Civil Engineering*, vol. 2018, Article ID 5459307, 10 pages, 2018.
- [38] Y. Wang, M. Fall, and A. Wu, “Initial temperature-dependence of strength development and self-desiccation in cemented paste backfill that contains sodium silicate,” *Cement and Concrete Composites*, vol. 67, no. 8, pp. 101–110, 2016.
- [39] F. Moghbel and M. Fall, “Response of compost biocover to freeze-thaw cycles: column experiments,” *Cold Regions Science and Technology*, vol. 131, no. 5, pp. 39–45, 2016.
- [40] W. Li, *Characteristics and Mechanism of Sulphate Effect on the Early Age Properties of Cemented Paste Backfill*, China University of Mining & Technology-Beijing, Beijing, China, 2016.
- [41] W. Li and M. Fall, “Sulphate effect on the early age strength and self-desiccation of cemented paste backfill,” *Construction and Building Materials*, vol. 106, no. 3, pp. 296–304, 2016.
- [42] J. C. H. Célestin and M. Fall, “Thermal conductivity of cemented paste backfill material and factors affecting it,” *International Journal of Surface Mining Reclamation & Environment*, vol. 23, no. 4, pp. 274–290, 2009.
- [43] H. Zhen and H. Liu, “Accurate measurement of static friction coefficient by inclined plane method,” *Modern Manufacturing Technology and Equipment*, vol. 28, no. 3, pp. 73–74, 2009.
- [44] L. Zhang, “Error handling for proving Newton’s second law with an inclined car,” *Education Teaching Forum*, vol. 21, no. 1, pp. 72–73, 2012.
- [45] C. Sun, F. Liu, M. Jiang, and H. Chen, “Size effect of compression strength and end constraint of rocks by distinct element simulation,” *Chinese Journal of Rock Mechanics & Engineering*, vol. 33, no. S2, pp. 3421–3428, 2014.